

Well-Posedness for Photoacoustic Tomography with Fabry–Perot Sensors*

Sebastian Acosta[†]

Abstract. In the mathematical analysis of photoacoustic imaging, it is usually assumed that the acoustic pressure (Dirichlet data) is measured on a detection surface. However, actual ultrasound detectors gather data of a different type. In this paper, we propose a more realistic mathematical model of ultrasound measurements acquired by the Fabry–Perot sensor. This modeling incorporates directional response of such sensors. We study the solvability of the resulting photoacoustic tomography problem, concluding that the problem is well-posed under certain assumptions. Numerical reconstructions are implemented using the Landweber iterations, after discretization of the governing equations using the finite element method.

Key words. thermoacoustic, imaging, inverse problems, Fabry–Perot sensor, ultrasound transducers

AMS subject classifications. 35R30, 35L05, 35R01, 92C55

DOI. 10.1137/19M1248297

1. Introduction. Photoacoustic tomography (PAT) is a hybrid imaging technique based on the photoacoustic effect, which is the transformation of absorbed electromagnetic energy into pressure waves. This technique takes advantage of the fact that absorption exhibits high contrast in soft biological tissues and that acoustic waves can be measured with broadband transducers leading to imaging with high resolution. Therefore, high-contrast and high resolution can be achieved simultaneously [14, 22, 23, 60, 67, 71, 72, 73, 74].

For qualitative PAT, the goal is to form an image of the initial state of the pressure field using boundary measurements of the transient pressure waves. Most of the reconstruction methods assume that the actual pressure field (Dirichlet data) can be measured at the boundary [2, 3, 4, 5, 11, 22, 32, 35, 36, 37, 38, 42, 44, 53, 54, 57, 61, 62, 63, 65]. In reality, ultrasound sensors are not able to measure the pressure field directly. Instead, they measure certain combinations of the field and its derivatives. This challenge has been noted in [79] and investigated by Finch [31] and by Zangerl, Moon, and Haltmeier [81].

Fabry–Perot transducers offer an alternative to piezoelectric sensors for ultrasound-based imaging applications [10, 16, 24, 34, 64, 80, 82]. The design consists of a sensing film (10–50 μm thick) sandwiched between extremely thin optically reflective coatings (≈ 50 nm thick) lying on an optically transparent backing substrate (≈ 2 cm thick). An illustration is shown in Figure 1. An interrogating laser beam is employed to generate reflections from both optically reflective coatings. When an incident pressure wave modulates the thickness of the sensing material, the change in the interference pattern from the reflected laser beam is used to

*Received by the editors March 11, 2019; accepted for publication (in revised form) July 31, 2019; published electronically October 1, 2019.

<https://doi.org/10.1137/19M1248297>

Funding: The work of the author was supported by National Science Foundation grant DMS-1712725.

[†]Predictive Analytics Lab, Baylor College of Medicine, and Texas Children’s Hospital, Houston, TX 77030 (sebastian.acosta@bcm.edu, <https://sites.google.com/site/acostasebastian01/>).

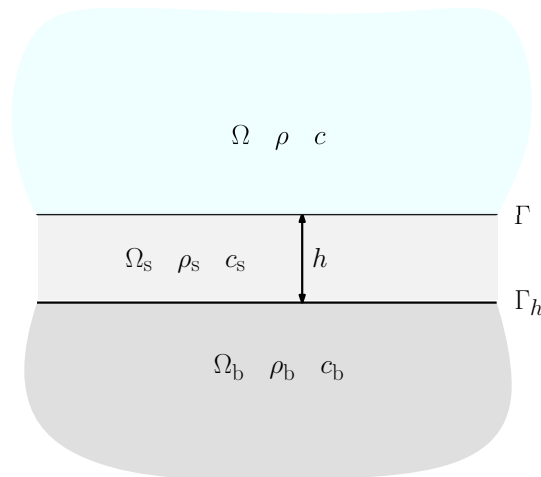


Figure 1. Diagram of domains and boundaries. Acoustic domain Ω with density ρ and wave speed c . Sensing film Ω_s of thickness $h > 0$, density ρ_s , and wave speed c_s . Backing substrate Ω_b with density ρ_b and wave speed c_b . The interface between the acoustic domain and the sensing film is denoted Γ . The interface between the sensing film and the backing substrate is denoted Γ_h .

estimate the distance between the reflective coatings. The deformation of the sensing material can then be related to pressure measurements. Cox and Beard provide a description of the Fabry–Perot design and an excellent study of its frequency and directional responses [24].

In this paper, we model and investigate the mathematical solvability of the PAT problem for measurements acquired by sensors based on the Fabry–Perot design. We model idealized point-like ultrasound transducers and the physical variable being measured by these sensors. Our goal is to determine whether such measurements lead to the mathematical solvability of the PAT problem. We shall not account for resolution limitations of the Fabry–Perot design due to finite-size sensing elements. We refer the reader to [24, 68, 76, 77] for investigations concerning this issue. Our modeling is further simplified by ignoring shear waves that can travel in the sensing material and its backing substrate. In other words, we develop an analysis based entirely on the scalar wave equation.

The acoustic domain Ω contains soft tissue with density ρ and wave speed c . The sensing film Ω_s of thickness $h > 0$ has density ρ_s and wave speed c_s . The backing substrate Ω_b has density ρ_b and wave speed c_b . We assume that ρ_s , ρ_b , c_s , and c_b are positive constants. However, ρ and c may vary within Ω . The interface between the acoustic domain and the sensing film is denoted Γ . The interface between the sensing film and the backing substrate is denoted Γ_h . Typically, the sensing film and the backing substrate are acoustically more rigid than the biological soft tissue of interest. Hence, the presence of the sensors induces partial reflections of the waves. Other researchers have investigated PAT with reflecting boundaries assuming that the actual pressure can be measured [2, 21, 28, 39, 45, 52]. Here we seek to incorporate in our model the influence that the sensor exerts on the pressure waves, as well as the nature of the acoustic measurements for the Fabry–Perot design. The interplay between the sensors and the pressure field is modeled by the following transmission conditions at the interface Γ ,

$$(1.1) \quad p = p_s \quad \text{and} \quad \frac{1}{\rho} \frac{\partial p}{\partial n} = \frac{1}{\rho_s} \frac{\partial p_s}{\partial n} \quad \text{on } \Gamma,$$

where p and p_s are the pressure in the acoustic medium and the sensing material, respectively. The first condition in (1.1), known as dynamic transmission, ensures the continuity of the pressure field. The second condition in (1.1), known as kinematic transmission, ensures the continuity of particle motion in the normal direction. Similar transmission conditions hold at the interface Γ_h ,

$$(1.2) \quad p_s = p_b \quad \text{and} \quad \frac{1}{\rho_s} \frac{\partial p_s}{\partial n} = \frac{1}{\rho_b} \frac{\partial p_b}{\partial n} \quad \text{on } \Gamma_h,$$

where p_b is the pressure in the backing substrate.

In order to simplify the analysis, in section 2 we derive an effective boundary condition (valid for small $h > 0$) to replace the transmission conditions (1.1)–(1.2). In section 3 we mathematically model the measurements acquired by ultrasound sensors based on the Fabry–Perot design. For the effective boundary condition and modeled boundary measurements, in section 4 we state and prove the solvability of the PAT problem. A reconstruction algorithm is proposed in section 5, where some numerical experiments are presented as well. The conclusions follow in section 6.

2. Effective boundary condition. For analytical and numerical purposes, it is convenient to replace the transmission conditions (1.1)–(1.2) for an asymptotically equivalent boundary condition for the acoustic pressure field at the boundary Γ . This condition is meant to account for the transmission into the sensing film Ω_s and into the backing substrate Ω_b without having to explicitly solve for the wave fields in those domains. See [7, 8, 18, 19, 41, 59], where similar problems are treated. This effective boundary condition also simplifies the model for the measurements as shown in section 3.

We proceed by making some geometric assumptions about the domain Ω_s occupied by the sensing film. We use the concept of *parallel surfaces* to define the shape of this extremely thin layer of material. These surfaces are parametrized by $0 < r < h$ and defined by $\Gamma_r = \{\mathbf{y} = \mathbf{x} + r\mathbf{n}(\mathbf{x}) : \mathbf{x} \in \Gamma\}$. For smooth Γ and sufficiently small h , each surface Γ_r is well-defined and smooth. Moreover, the normal vector $\mathbf{n}(\mathbf{x} + r\mathbf{n}(\mathbf{x}))$ of the parallel surface Γ_r coincides with the normal vector $\mathbf{n}(\mathbf{x})$ of Γ for each $\mathbf{x} \in \Gamma$. We let Ω_s be the union of this family of parallel surfaces, where h being sufficiently small ensures that each point $\mathbf{y} \in \Omega_s$ can be uniquely represented in the form $\mathbf{y} = \mathbf{x} + r\mathbf{n}(\mathbf{x})$ for $\mathbf{x} \in \Gamma$ and $0 < r < h$. See details in [43, sect. 6.2] and [26, Probl. 11, sect. 3.5].

The pressure field p_s in the sensing material satisfies the wave equation,

$$(2.1) \quad c_s^{-2} \frac{\partial^2 p_s}{\partial t^2} = \frac{\partial^2 p_s}{\partial n^2} + 2\mathcal{H}_r \frac{\partial p_s}{\partial n} + \Delta_{\Gamma_r} p_s \quad \text{in } (0, T) \times \Omega_s.$$

For convenience, we have expressed the Laplacian in Ω_s using the normal derivative $\partial/\partial n$ (which makes sense at any point in Ω_s given its definition in terms of parallel surfaces), the mean curvature \mathcal{H}_r of Γ_r , and the Laplace–Beltrami operator Δ_{Γ_r} associated with Γ_r . See

details in [9]. As in [24], we assume that the pressure field p_b in the backing substrate is outgoing. Therefore, the pressure field p_b satisfied the following radiation condition:

$$(2.2) \quad \frac{\partial p_b}{\partial n} = \Lambda_{b,h} p_b \quad \text{on } \Gamma_h,$$

where $\Lambda_{b,h}$ is a nonreflecting boundary operator. The subject of nonreflecting or absorbing boundary conditions is beyond the scope of this paper. We refer to [9, 13, 6, 20, 1] for some relevant articles on that topic. We consider

$$(2.3) \quad \Lambda_{b,h} = -c_b^{-1} \partial_t - \mathcal{H}_h,$$

which is derived in [9] as a first order nonreflecting condition that takes into account the mean curvature \mathcal{H}_h of the boundary Γ_h . As shown in [43, sect. 6.2] or [26, Probl. 11, sect. 3.5], the mean curvatures \mathcal{H} and \mathcal{H}_h of the surfaces Γ and Γ_h , respectively, are related by

$$\mathcal{H}_h = \frac{\mathcal{H} + h\mathcal{K}}{1 + 2h\mathcal{H} + h^2\mathcal{K}} = \mathcal{H} + h(\mathcal{K} - 2\mathcal{H}^2) + \mathcal{O}(h^2),$$

where \mathcal{K} is the Gaussian curvature of Γ . Notice that we are using the mean curvature sign convention from [9], not from [43] or [26]. Therefore, we have that at the surface Γ , the associated nonreflecting operator Λ_b given by

$$(2.4) \quad \Lambda_b = -c_b^{-1} \partial_t - \mathcal{H}$$

satisfies $\Lambda_{b,h} = \Lambda_b + h(\mathcal{K} - 2\mathcal{H}^2) + \mathcal{O}(h^2)$, where $\Lambda_{b,h}$ is defined in (2.3).

We proceed with a Taylor expansion for the normal derivative of the pressure field,

$$\begin{aligned} \frac{1}{\rho} \frac{\partial p}{\partial n} \Big|_{\Gamma} &= \frac{1}{\rho_s} \frac{\partial p_s}{\partial n} \Big|_{\Gamma} = \frac{1}{\rho_s} \left[\frac{\partial p_s}{\partial n} \Big|_{\Gamma_h} - h \frac{\partial^2 p_s}{\partial n^2} \Big|_{\Gamma} \right] + \mathcal{O}(h^2) \\ &= \frac{1}{\rho_s} \left[\frac{\rho_s}{\rho_b} \Lambda_{b,h} \left(p_s + h \frac{\partial p_s}{\partial n} \right) \Big|_{\Gamma} - h \frac{\partial^2 p_s}{\partial n^2} \Big|_{\Gamma} \right] + \mathcal{O}(h^2) \\ &= \frac{1}{\rho_s} \left[\frac{\rho_s}{\rho_b} \Lambda_{b,h} \left(p + h \frac{\rho_s}{\rho} \frac{\partial p}{\partial n} \right) \Big|_{\Gamma} - h \left(c_s^{-2} \partial_t^2 p - 2\mathcal{H} \frac{\rho_s}{\rho} \frac{\partial p}{\partial n} - \Delta_{\Gamma} p \right) \Big|_{\Gamma} \right] + \mathcal{O}(h^2), \end{aligned}$$

where we have employed the transmission conditions (1.1)–(1.2), the wave equation (2.1), and the radiation condition (2.2). Using (2.4), regrouping terms and neglecting $\mathcal{O}(h^2)$ terms, we obtain a first order boundary condition

$$(2.5) \quad \frac{1}{\rho} \frac{\partial p}{\partial n} - \frac{1}{\rho_b} \Lambda_b p = h \left[\frac{\rho_s}{\rho \rho_b} \Lambda_b \frac{\partial p}{\partial n} + \frac{1}{\rho_b} (\mathcal{K} - 2\mathcal{H}^2) p - \frac{1}{\rho_s} \left(c_s^{-2} \partial_t^2 p - 2\mathcal{H} \frac{\rho_s}{\rho} \frac{\partial p}{\partial n} - \Delta_{\Gamma} p \right) \right]$$

for the acoustic wave field p on the surface Γ . This conditions implies that most of the influence (zeroth order terms) that the sensor exerts on the pressure field at the boundary is provided by the thick backing substrate which reflects and refracts the wave field according to the mismatch in densities ρ and ρ_b , and in wave speeds c and c_b . The presence of the

thin sensing film is accounted for by the first order terms in (2.5). If these latter terms are neglected, the pressure field satisfies the following zeroth order effective boundary condition:

$$(2.6) \quad \frac{1}{\rho} \frac{\partial p}{\partial n} = \frac{1}{\rho_b} \Lambda_b p \quad \text{on } \Gamma.$$

However, the terms of order $\mathcal{O}(h)$ in (2.5) become important in section 3, where we model the ultrasound measurements which are of order $\mathcal{O}(h)$.

3. Modeling ultrasound measurements. For an ultrasound sensor based on the Fabry–Perot design, the quantity being measured is proportional to the difference in the normal projection of the particle displacement on both sides of the sensing film [24]. Hence, up to a constant of proportionality, the measurements \mathbf{m} acquired by the ultrasound transducer satisfy

$$(3.1) \quad \partial_t^2 \mathbf{m} \sim \left(\partial_t^2 \mathbf{u}_s|_{\Gamma} - \partial_t^2 \mathbf{u}_s|_{\Gamma_h} \right) \cdot \mathbf{n} = \frac{1}{\rho_s} \left(\frac{\partial p_s}{\partial n} \Big|_{\Gamma_h} - \frac{\partial p_s}{\partial n} \Big|_{\Gamma} \right),$$

where the symbol \sim means equality up to a multiplicative constant, and the pressure–displacement formulation is valid in the absence of shear stress. We seek to express the measurement in terms of the pressure in the acoustic medium only. Using the transmission conditions (1.1)–(1.2) at both sides of the sensing film, and (2.2)–(2.4), we obtain

$$(3.2) \quad \begin{aligned} \frac{\partial p_s}{\partial n} &= \frac{\rho_s}{\rho} \frac{\partial p}{\partial n} \quad \text{on } \Gamma, \\ \frac{\partial p_s}{\partial n} &= \frac{\rho_s}{\rho_b} \frac{\partial p_b}{\partial n} = \frac{\rho_s}{\rho_b} \Lambda_{b,h} p_b = \frac{\rho_s}{\rho_b} \Lambda_{b,h} p_s = \frac{\rho_s}{\rho_b} [\Lambda_b + h(\mathcal{K} - 2\mathcal{H}^2)] p_s \quad \text{on } \Gamma_h. \end{aligned}$$

We make the following Taylor approximation for the pressure field p_s within the sensing film and combine it with (1.1)–(1.2) and (3.2) to obtain

$$(3.3) \quad p_s|_{\Gamma_h} = \left[p_s + h \frac{\partial p_s}{\partial n} \right] \Big|_{\Gamma} + \mathcal{O}(h^2) = \left[p + h \frac{\rho_s}{\rho} \frac{\partial p}{\partial n} \right] \Big|_{\Gamma} + \mathcal{O}(h^2).$$

Therefore, combining (3.1)–(3.3) we obtain an expression for the measurements in terms of the acoustic pressure field (Dirichlet data) and its normal derivative (Neumann data) at the boundary Γ as follows:

$$(3.4) \quad \partial_t^2 \mathbf{m} \sim \left(\frac{1}{\rho_b} \Lambda_b p - \frac{1}{\rho} \frac{\partial p}{\partial n} \right) + h \left[\frac{\rho_s}{\rho \rho_b} \Lambda_b \frac{\partial p}{\partial n} + (\mathcal{K} - 2\mathcal{H}^2) p \right] + \mathcal{O}(h^2).$$

Neglecting the $\mathcal{O}(h^2)$ terms on the right-hand side of (3.4) and using the effective boundary conditions (2.5)–(2.6), we obtain a simplified or first order model for the measurements

$$(3.5) \quad \partial_t^2 \mathbf{m} \sim \partial_t^2 p + 2\mathcal{H} \frac{\rho_s}{\rho_b} \frac{c_s^2}{c_b} \partial_t p + 2\mathcal{H}^2 c_s^2 \frac{\rho_s}{\rho_b} p - c_s^2 \Delta_{\Gamma} p \quad \text{on } (0, T) \times \Gamma,$$

where we have used the definition of the operator Λ_b given by (2.4). In order to fully determine \mathbf{m} , initial conditions must be provided. Consistent with the PAT scenario, where the pressure field has vanishing initial Cauchy data in the exterior of Ω , we let $\mathbf{m} = \partial_t \mathbf{m} = 0$ on $\{t = 0\} \times \Gamma$.

To illustrate the response associated with this sensor design, we briefly analyze its behavior for plane waves. For convenience, we momentarily assume that Γ is a plane through the origin. Both the effective boundary condition (2.6) and the form of the measurements (3.5) play a role in this analysis. From (2.4) we have $\Lambda_b = -c_b^{-1} \partial_t$ because for a flat surface Γ the mean curvature is $\mathcal{H} = 0$. A plane wave $p_{\text{inc}} = e^{i(\mathbf{x} \cdot \mathbf{k} - \omega t)}$ with incidence angle θ induces a reflection governed by the effective boundary condition (2.6). The superposition of the incident and reflected waves has the form

$$(3.6) \quad p(\mathbf{x}, t) = e^{i(\mathbf{x} \cdot \mathbf{k} - \omega t)} + R e^{i(\mathbf{x} \cdot \mathbf{k}_r - \omega t)},$$

where R is the reflection coefficient, \mathbf{k}_r is the reflection wavenumber, such that $|\mathbf{k}| = |\mathbf{k}_r| = \omega/c$, and $\mathbf{n} \cdot \mathbf{k}_r = -\mathbf{n} \cdot \mathbf{k}$, where \mathbf{n} is the outward normal vector. We also have $\mathbf{n} \cdot \mathbf{k} = |\mathbf{k}| \cos \theta$. Once (3.6) is plugged into (2.6), the reflection coefficient is shown to satisfy

$$(3.7) \quad R = \frac{\cos \theta - \alpha}{\cos \theta + \alpha}, \quad \text{where} \quad \alpha = \frac{\rho c}{\rho_b c_b}.$$

Plugging (3.6)–(3.7) into (3.5) and evaluating at the origin $\mathbf{x} = \mathbf{0}$, we find that the measurements satisfy

$$(3.8) \quad \frac{\mathbf{m}}{p_{\text{inc}}} \sim \left(1 + \frac{\cos \theta - \alpha}{\cos \theta + \alpha}\right) \left(1 - \frac{c_s^2}{c^2} \sin^2 \theta\right).$$

Figure 2 displays the directional response (3.8) for plane waves as a function of the incidence angle θ . The parameters were taken from [24] for a Parylene sensing film and polycarbonate backing substrate. Figure 2 shows that incidence at approximately 42.99° corresponds

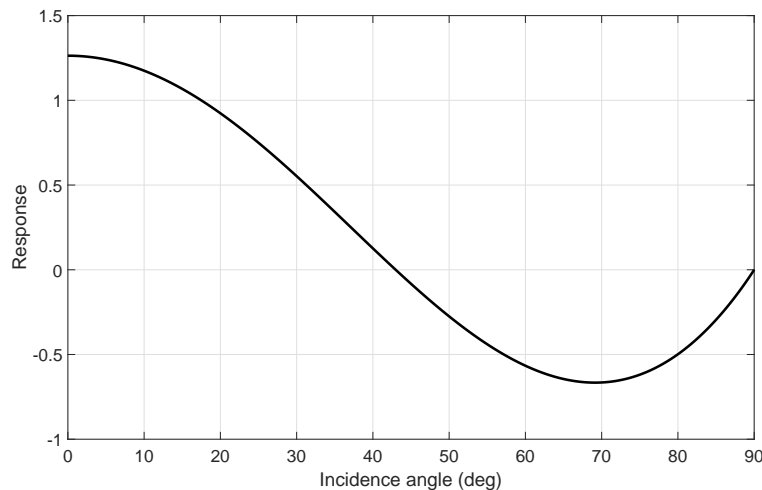


Figure 2. Directional response of Fabry–Perot measurements for plane waves. The parameters, taken from [24], correspond to a Parylene sensing film with (compressional) wave speed $c_s = 2200$ m/s and density $\rho_s = 1180$ kg/m³ and a polycarbonate backing substrate with (compressional) wave speed $c_b = 2180$ m/s and density $\rho_b = 1180$ kg/m³. The acoustic medium corresponds to water with wave speed $c = 1500$ m/s and density $\rho = 1000$ kg/m³.

to a critical angle where the waves cause no particle motion in the normal direction. This occurs when the tangential phase speed of the acoustic wave equals the wave speed in the sensing film. The Fabry-Perot sensor does not capture such acoustic waves. We also note that for incidence angles greater than this critical angle, the pressure wave and the measurement have opposite signs. The response also approaches zero as the incidence angle approaches 90° . Therefore, for incidence at tangential angles, the sensor design is not able to measure the pressure waves adequately.

The above are some of the features not taken into account when it is assumed that the actual pressure field (Dirichlet data) is acquired at the measurement boundary. As explained in the introduction, the overly idealized assumption for ultrasound sensors is that they measure the pressure field at the boundary and that the sensors themselves do not perturb the pressure waves. This overly idealized model can be expressed as follows:

$$(3.9) \quad \mathbf{m} \sim p \quad \text{on } (0, T) \times \Gamma, \quad \text{and } \rho_s = \rho_b = \rho \text{ and } c_s = c_b = c.$$

4. Main mathematical results. Here we define the PAT problem in terms of the wave equation, the effective boundary condition (2.6), and the ultrasound measurements modeled by (3.5). We also prove the solvability of this problem under the following geometric condition for the wave speed c and the domain Ω .

Assumption 4.1 (nontrapping condition). Let Ω be a simply connected bounded domain with smooth boundary Γ . Assume there exists $T_o < \infty$ such that any geodesic ray of the manifold $(\Omega, c^{-2}dx^2)$, originating from any point in Ω at time $t = 0$, reached the boundary Γ at a nondiffractive point before $t = T_o$.

The forward mapping, which we seek to invert, is given by

$$(4.1) \quad \mathcal{F} : (p_0, p_1) \mapsto \mathbf{m},$$

where the measurement \mathbf{m} satisfies (3.5) with vanishing initial Cauchy data. The initial velocity p_1 is known to be zero in the context of PAT. However, the mathematical theory allows us to recover it as well. The pressure field p solves the following initial boundary value problem:

$$(4.2) \quad \begin{aligned} \partial_t^2 p &= c^2 \Delta p && \text{in } (0, T) \times \Omega, \\ \rho_b \partial_n p &= \rho \Lambda_b p && \text{on } (0, T) \times \Gamma, \\ p &= p_0 \quad \text{and} \quad \partial_t p = -p_1 && \text{on } \{t = 0\} \times \Omega. \end{aligned}$$

The well-posedness of this problem for $(p_0, p_1) \in H_0^1(\Omega) \times H^0(\Omega)$ has been established. See, for instance, [30, 46, 47]. The unique solution satisfies $p \in C([0, T]; H^1(\Omega))$, $\partial_t p \in C([0, T]; H^0(\Omega))$, $p|_\Gamma \in H^1((0, T) \times \Gamma)$, and $\partial_n p \in H^0((0, T) \times \Gamma)$. We work with the standard Sobolev spaces based on square-integrable functions over Ω or $(0, T) \times \Gamma$. The associated inner-product extends naturally as the duality pairing between functionals and functions. We should interpret the Hilbert space $H^0(\Omega)$ with the inner-product appropriately weighted by c^{-2} so that $c^2 \Delta$ is formally self-adjoint with respect to the duality pairing of $H^0(\Omega)$.

Now we state our main result in the form of a theorem.

Theorem 4.2 (main result). *Under the nontrapping Assumption 4.1 for the manifold $(\Omega, c^{-2}dx^2)$ and time $T > T_0$, the forward mapping $\mathcal{F} : H_0^1(\Omega) \times H^0(\Omega) \rightarrow H^0((0, T); H^1(\Gamma))$ is injective, that is, the PAT problem is uniquely solvable. Moreover, the following stability estimate holds:*

$$(4.3) \quad \|(p_0, p_1)\|_{H^0(\Omega) \times H^{-1}(\Omega)} \leq C \|\mathbf{m}\|_{H^0((0, T); H^1(\Gamma))}$$

for some constant $C > 0$.

We proceed to prove this theorem by showing that the adjoint of the forward mapping is surjective. This adjoint mapping \mathcal{F}^* is given by

$$(4.4) \quad \mathcal{F}^* : \psi \mapsto (\partial_t \xi(0), \xi(0)),$$

where ξ solves the following backward-in-time boundary value problem:

$$(4.5) \quad \begin{aligned} \partial_t^2 \xi &= c^2 \Delta \xi && \text{in } (0, T) \times \Omega, \\ \rho_b \partial_n \xi - \rho \Lambda_b^* \xi &= \rho_b (\partial_t^2 + a \partial_t + b - c_s^2 \Delta_\Gamma)^* (\partial_t^{-2})^* \psi && \text{on } (0, T) \times \Gamma, \\ \xi &= 0 \quad \text{and} \quad \partial_t \xi = 0 && \text{on } \{t = T\} \times \Omega, \end{aligned}$$

where $a = 2\mathcal{H}c_s^2\rho_s/(c_b\rho_b)$ and $b = 2\mathcal{H}^2c_s^2\rho_s/\rho_b$ are constants. The operator ∂_t^{-2} can be defined as

$$(4.6) \quad (\partial_t^{-2}v)(t) = \int_0^t \int_0^\tau v(s) ds d\tau.$$

Notice that $\partial_t^{-2}\partial_t^2v = \partial_t^2\partial_t^{-2}v = v$ for all sufficiently smooth v such that $v|_{t=0} = \partial_tv|_{t=0} = 0$. Also notice that ∂_t^2 is formally self-adjoint. In particular,

$$(4.7) \quad (\partial_t^2v, \phi)_{H^0((0, T) \times \Gamma)} = (v, \partial_t^2\phi)_{H^0((0, T) \times \Gamma)}$$

for all sufficiently regular v and ϕ such that $v|_{t=0} = \partial_tv|_{t=0} = 0$ and $\phi|_{t=T} = \partial_t\phi|_{t=T} = 0$. The Laplace–Beltrami operator Δ_Γ is also self-adjoint since the manifold Γ has no boundary. The nonreflecting operator Λ_b defined in (2.4) has an adjoint given by $\Lambda_b^* = c_b^{-1}\partial_t - \mathcal{H}$. Therefore, it stays as a differential operator with first and zeroth order terms.

The statement of Theorem 4.2 is a direct consequence of the following lemma.

Lemma 4.3. *Under the nontrapping Assumption 4.1 for the manifold $(\Omega, c^{-2}dx^2)$ and time $T > T_0$, the operator $\mathcal{F}^* : H^0((0, T); H^{-1}(\Gamma)) \rightarrow H^0(\Omega) \times H^1(\Omega)$ is surjective.*

Proof. The mapping \mathcal{F}^* can be composed as $\mathcal{F}^* = \mathcal{G}_2 \circ \mathcal{G}_1$, where

$$(4.8) \quad \begin{aligned} \mathcal{G}_1 : \psi &\mapsto \varphi, \\ \mathcal{G}_2 : \varphi &\mapsto (\partial_t \xi(0), \xi(0)), \end{aligned}$$

where the mapping \mathcal{G}_1 is given by

$$(4.9) \quad \varphi = \partial_t^2 \Psi - a \partial_t \Psi + b \Psi - c_s^2 \Delta_\Gamma \Psi \quad \text{in } (0, T) \times \Gamma,$$

where Ψ has vanishing Cauchy data at $t = T$ and solves $\partial_t^2 \Psi = \rho_b \psi$. The mapping \mathcal{G}_2 is defined via ξ , the solution of

$$(4.10) \quad \begin{aligned} \partial_t^2 \xi &= c^2 \Delta \xi && \text{in } (0, T) \times \Omega, \\ \rho_b \partial_n \xi - \rho \Lambda_b^* \xi &= \varphi && \text{on } (0, T) \times \Gamma, \\ \xi = 0 \quad \text{and} \quad \partial_t \xi &= 0 && \text{on } \{t = T\} \times \Omega. \end{aligned}$$

Under the nontrapping assumption, the mapping $\mathcal{G}_2 : \varphi \mapsto (\partial_t \xi(0), \xi(0))$ defined by (4.10) is well-known to be surjective from $H^0((0, T); H^0(\Gamma))$ onto $H^0(\Omega) \times H^1(\Omega)$. That is the central theme of exact boundary controllability for the wave equation. See [33, Chap. 6] and [12, Cor. 4.10].

Hence, it only remains to show that the mapping \mathcal{G}_1 is surjective. This can be accomplished by proving that (4.9) is solvable for any forcing term $\varphi \in H^0((0, T); H^0(\Gamma))$ such that Ψ has vanishing Cauchy data at $t = T$ and $\partial_t^2 \Psi \in H^0((0, T); H^{-1}(\Gamma))$. This solvability is a well-established result. See [30, sect. 7.2 Theorems 3–5], [46], and [47, Chap. 3, sect. 8, Thm. 8.1]. As a consequence, the operator \mathcal{F}^* is surjective from $H^0((0, T); H^{-1}(\Gamma))$ onto $H^0(\Omega) \times H^1(\Omega)$. ■

Lemma 4.3 renders the proof of **Theorem 4.2**. Indeed, we first notice that since $\mathcal{F}^* : H^0((0, T); H^{-1}(\Gamma)) \rightarrow H^0(\Omega) \times H^1(\Omega)$ is well-defined and surjective, then $\mathcal{F} : H^0(\Omega) \times H^{-1}(\Omega) \rightarrow H^0((0, T); H^1(\Gamma))$ is well-defined, is injective, and has a closed range. The stability estimate (4.3) then follows from the open mapping theorem (see [50, Chap. 2] or [27, Chap. 2]).

5. Numerical results. In this section we implement reconstruction algorithms to solve the PAT problem at the discrete level. The reconstructions are based on the Landweber iterative method [29, Chap. 6]. In the context of PAT, the Landweber iteration has been employed previously because of its simplicity and compatibility with regularization methods [17, 25, 35, 36, 37, 54, 66]. Other approaches, such as the conjugate gradient method, may also be employed to solve PAT problems [2, 3, 37, 51, 54, 68, 69, 70, 78]. The Landweber iteration is defined in **Algorithm 5.1**.

Algorithm 5.1. Landweber iteration.

```

Initial guess  $\phi_0 = 0$ .
Set  $0 < \gamma < \|\mathcal{F}\|^{-2}$ .
for  $k = 0, 1, 2, \dots$  do
     $\phi_{k+1} = \phi_k - \gamma \mathcal{F}^* (\mathcal{F} \phi_k - \mathbf{m})$ 
end for

```

The discretizations of the forward map (4.1) and adjoint map (4.4) are based on a piecewise linear finite element method (FEM) and second order finite difference for the time derivatives in the initial boundary value problems (4.2) and (4.5), respectively. The discretization parameters were chosen to satisfy the CFL stability condition. The FEM was implemented on triangular meshes of the unit disk and the physical parameters, described in **Figure 2**, were nondimensionalized accordingly. **Figure 3** shows a coarse triangular mesh and the Shepp–Logan phantom to be reconstructed. Measured data was synthetically generated by discretizing the forward operator \mathcal{F} using the FEM method. In all simulations, the mesh employed to

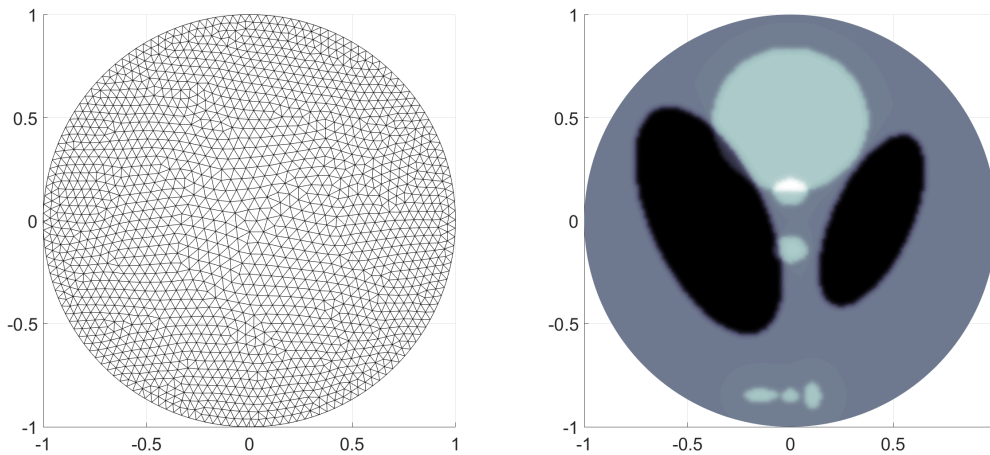


Figure 3. Coarse triangulation for the FEM (left) and exact profile to be reconstructed (right).

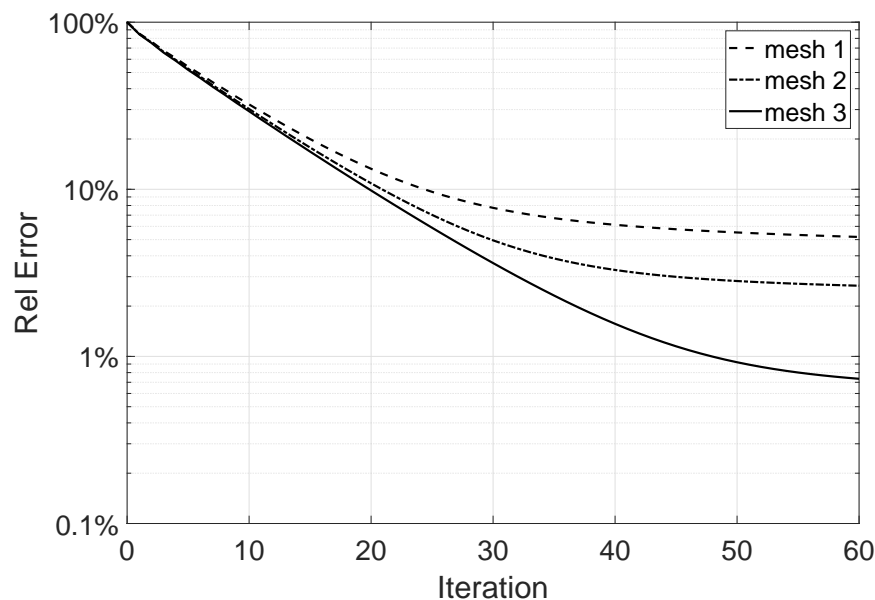


Figure 4. Relative error for the Landweber iterations. The physical parameters, same as in [Figure 2](#), were nondimensionalized for these simulations. The mesh refinement leads to the numbers of degrees of freedom 1713, 6875, and 27248 for the meshes 1, 2, and 3, respectively. This corresponds to halving the mesh size in consecutive refinements.

generate the measurements had mesh size about half of the mesh size for the mesh employed to reconstruct the phantom.

[Figure 4](#) displays the error $\|\phi_k - p_0\|$ (where p_0 is the exact solution) as a function of the iteration number $k \geq 0$ of the Landweber method. The figure shows results for three FEM

meshes that were consecutively refined by halving the mesh size. We notice that initially, the error decays exponentially in k (as the theory of this method predicts) but then it stagnates. The stagnation level decreases with mesh refinement. This phenomenon may be attributed to the fact that the discrete version of \mathcal{F}^* is not the actual adjoint of the discrete version of \mathcal{F} . Thus, the discretization of the normal operator $\mathcal{F}^*\mathcal{F}$ is not symmetric positive definite as this method requires. However, as the mesh is refined, we expect this error to reduce. Implementation of an exact numerical adjoint, as done by Huang et al. [40], could remedy this issue.

Last, we compare the reconstruction of the initial pressure profile obtained by accounting for the structure of the Fabry–Perot measurement model (3.5) against the reconstruction obtained from the overly idealized (but commonly assumed) model (3.9). The latter reconstruction is obtained by synthetically producing the measurements following the model (3.5), but then incorrectly assuming that the measurements satisfy (3.9). Figure 5 displays the reconstruction results for both measurement models using 60 iterations of the Landweber method. For the reconstruction following the proposed model (3.5), the relative error is 0.73%. For the reconstruction following the overly idealized model (3.9), the relative error is 23.02%.

6. Conclusions. We have developed a model for the type of measurements acquired by sensors based on the Fabry–Perot design. This model takes the form shown in (3.5). The validity of this expression is limited to small values for the thickness h of the sensing film with respect to the wavelength of the pressure fields. This means that $h \ll c_s/f$, where f is the oscillatory frequency. For instance, [24] considered a Fabry–Perot polymer film of thickness $h = 40 \mu\text{m}$ with compressional wave speed $c_s = 2200 \text{ m/s}$ and a frequency range 1–15 MHz. At the higher end of this range, the film thickness is about one fourth of the wavelength. Therefore, the proposed model would be valid for most of this frequency range.

Our mathematical model of the measurements captures the directional response observed experimentally [24, 34, 64, 80, 82]. For instance, notice that for a pressure wave p impinging the boundary Γ in the normal direction, the sensor design fully captures the pressure field. However, for pressure waves traveling at other incidence angles, the sensor response may exhibit nonideal behavior, such as vanishing response at critical angles, as shown in Figure 2. This is the mathematical description of the directivity associated with these ultrasound sensors. The incorporation of these features into reconstruction algorithms has been recognized as one of the challenges associated with improving photoacoustic inversion [22, 28, 68, 76].

Using the model (3.5) for the measurements, we studied the solvability of the PAT problem and concluded that the problem is well-posed in the appropriate spaces and norms. See the precise statements in Theorem 4.2. Following the analysis, a reconstruction algorithm was implemented based on the Landweber iteration. We carried out proof-of-concept numerical simulations to illustrate the reconstructions obtained from this method for synthetic data after discretization using FEM. For the chosen Shepp–Logan phantom, Figure 5 displays the results obtained by incorporating (panel A) and by ignoring (panel B) the model for the Fabry–Perot measurements. The respective error profiles are shown in panels C and D of the same figure. Approximately, a 22% relative error is added when the proposed model for the Fabry–Perot measurement is not incorporated in the reconstruction algorithm. We also highlight the qualitative difference between the error profiles from panels C and D of Figure 5. By ignoring

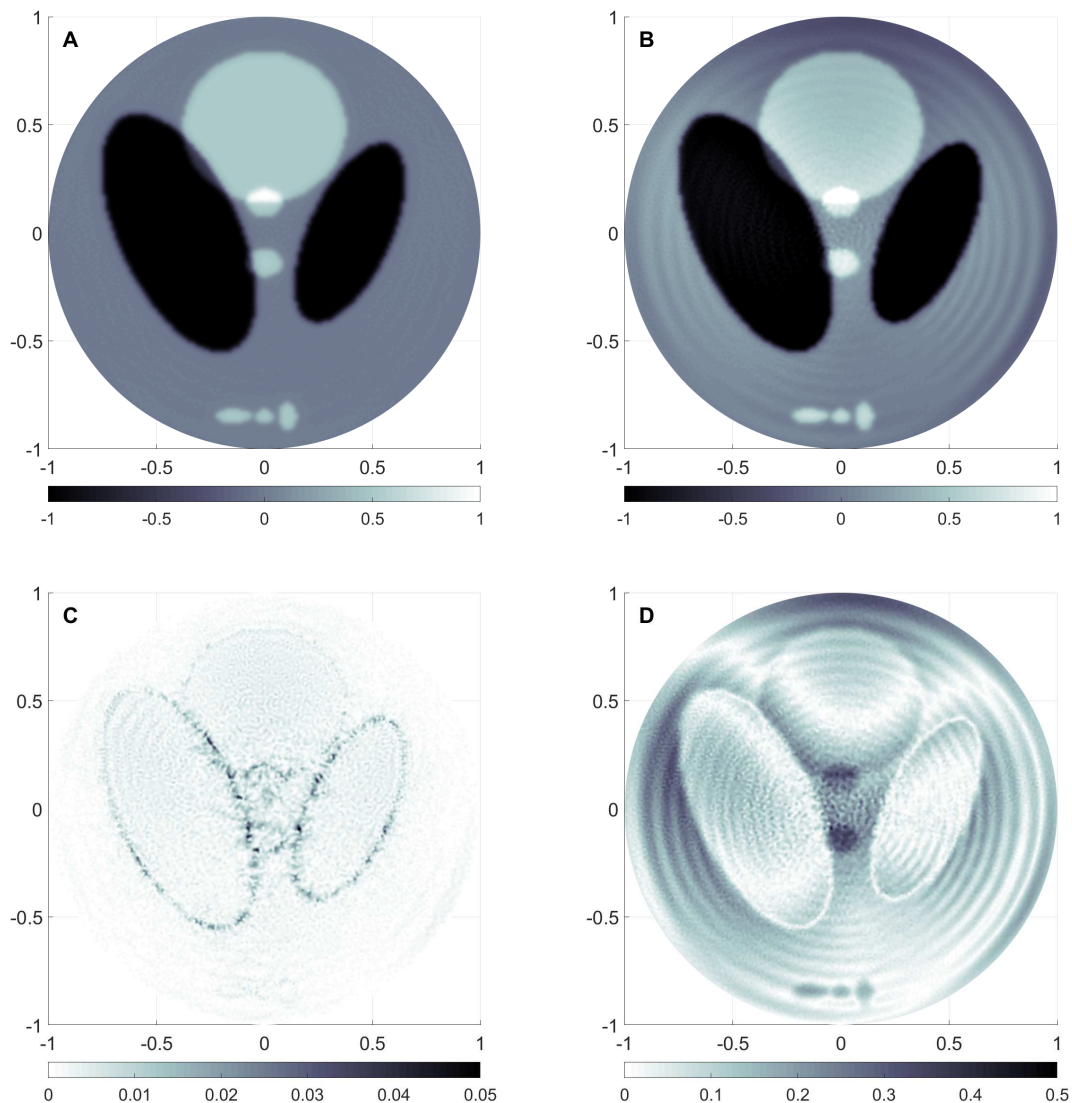


Figure 5. Panel A: Reconstruction accounting for the measured data of the Fabry–Perot sensor as modeled by (3.5). Panel B: Reconstruction obtained using the overly idealized (but commonly assumed) model of measured data (3.9). Panel C: Error profile for the reconstruction shown in panel A. Panel D: Error profile for the reconstruction shown in panel B.

the Fabry–Perot model, the error profile exhibits prominent artifacts over the entire image, especially near the detection boundary. These artifacts may be explained by the directivity response shown in Figure 2. By design, the proposed reconstruction algorithm accounts for the directivity response of these sensors leading to the removal of those artifacts.

Finally, we propose a couple of directions for future research that may improve or extend this work. It remains to study the well-posedness of the PAT problem for a Fabry–Perot

measurement model that includes both the p-waves and s-waves in the elastic sensing film and backing substrate of the sensor. Such a model would incorporate the influence of the shear waves on the measurements as studied by Cox and Beard for plane waves [24]. Also, nontrivial directivity responses are induced not only by the Fabry–Perot sensor design but also by piezoelectric detectors [15, 55, 56, 58, 75]. Therefore, analysis of the well-posedness for the PAT problem using piezoelectric measurements is also needed.

Acknowledgments. The author would like to thank Texas Children’s Hospital for its support and for the research-oriented environment provided by the Predictive Analytics Lab. The author would like to thank the anonymous referees for carefully reviewing the manuscript and for providing helpful recommendations.

REFERENCES

- [1] S. ACOSTA, *High order surface radiation conditions for time-harmonic waves in exterior domains*, Comput. Methods Appl. Mech. Engrg., 322 (2017), pp. 296–310, <https://doi.org/10.1016/j.cma.2017.04.032>.
- [2] S. ACOSTA AND C. MONTALTO, *Multiwave imaging in an enclosure with variable wave speed*, Inverse Problems, 31 (2015), 065009, <https://doi.org/10.1088/0266-5611/31/6/065009>.
- [3] S. ACOSTA AND C. MONTALTO, *Photoacoustic imaging taking into account thermodynamic attenuation*, Inverse Problems, 32 (2016), 115001, <https://doi.org/10.1088/0266-5611/32/11/115001>.
- [4] S. ACOSTA AND B. PALACIOS, *Thermoacoustic tomography for an integro-differential wave equation modeling attenuation*, J. Differential Equations, 264 (2018), pp. 1984–2010, <https://doi.org/10.1016/j.jde.2017.10.012>.
- [5] M. AGRANOVSKY, P. KUCHMENT, AND L. KUNYANSKY, *On reconstruction formulas and algorithms for the thermoacoustic tomography*, in Photoacoustic Imaging and Spectroscopy, CRC Press, Boca Raton, FL, 2009, pp. 89–101.
- [6] X. ANTOINE, *Advances in the on-surface radiation condition method: Theory, numerics and applications*, in Computational Methods for Acoustics Problems, Saxe-Coburg Publications, Stirlingshire, UK, 2008, pp. 169–194.
- [7] X. ANTOINE AND H. BARUCQ, *Approximation by generalized impedance boundary conditions of a transmission problem in acoustic scattering*, Math. Model. Numer. Anal., 39 (2005), pp. 1041–1059, <https://doi.org/10.1051/m2an:2005037>.
- [8] X. ANTOINE AND H. BARUCQ, *On the construction of approximate boundary conditions for solving the interior problem of the acoustic scattering transmission problem*, in Domain Decomposition Methods in Science and Engineering, Springer, Berlin, 2005, pp. 133–140, https://doi.org/10.1007/3-540-26825-1_9.
- [9] X. ANTOINE, H. BARUCQ, AND A. BENDALI, *Bayliss-Turkel-like radiation conditions on surfaces of arbitrary shape*, J. Math. Anal. Appl., 229 (1999), pp. 184–211, <https://doi.org/10.1006/jmaa.1998.6153>.
- [10] S. ARRIDGE, P. BEARD, M. BETCKE, B. COX, N. HUYNH, F. LUCKA, O. OGUNLADE, AND E. ZHANG, *Accelerated high-resolution photoacoustic tomography via compressed sensing*, Phys. Medicine Biol., 61 (2016), pp. 8908–8940, <https://doi.org/10.1088/1361-6560/61/24/8908>.
- [11] S. R. ARRIDGE, M. M. BETCKE, B. T. COX, F. LUCKA, AND B. E. TREEBY, *On the adjoint operator in photoacoustic tomography*, Inverse Problems, 32 (2016), 115012, <https://doi.org/10.1088/0266-5611/32/11/115012>.
- [12] C. BARDOS, G. LEBEAU, AND J. RAUCH, *Sharp sufficient conditions for the observation, control, and stabilization of waves from the boundary*, SIAM J. Control Optim., 30 (1992), pp. 1024–1065, <https://doi.org/10.1137/0330055>.
- [13] H. BARUCQ, J. DIAZ, AND V. DUPRAT, *Micro-differential boundary conditions modelling the absorption of acoustic waves by 2D arbitrarily-shaped convex surfaces*, Commun. Comput. Phys., 11 (2012), pp. 674–690, <https://doi.org/10.4208/cicp.311209.260411s>.

- [14] P. BEARD, *Biomedical photoacoustic imaging*, Interface Focus, 1 (2011), pp. 602–631, <https://doi.org/10.1098/rsfs.2011.0028>.
- [15] P. BEARD, A. HURRELL, AND T. MILLS, *Characterization of a polymer film optical fiber hydrophone for use in the range 1 to 20 MHz: A comparison with PVDF needle and membrane hydrophones*, IEEE Trans. Ultrason. Ferroelectr. Freq. Control, 47 (2000), pp. 256–264, <https://doi.org/10.1109/58.818769>.
- [16] P. BEARD, F. PERENNES, AND T. MILLS, *Transduction mechanisms of the Fabry-Perot polymer film sensing concept for wideband ultrasound detection*, IEEE Trans. Ultrason. Ferroelectr. Freq. Control, 46 (1999), pp. 1575–1582, <https://doi.org/10.1109/58.808883>.
- [17] Z. BELHACHMI, T. GLATZ, AND O. SCHERZER, *A direct method for photoacoustic tomography with inhomogeneous sound speed*, Inverse Problems, 32 (2016), 045005, <https://doi.org/10.1088/0266-5611/32/4/045005>.
- [18] A. BENDALI AND K. LEMRABET, *The effect of a thin coating on the scattering of a time-harmonic wave for the Helmholtz equation*, SIAM J. Appl. Math., 56 (1996), pp. 1664–1693, <https://doi.org/10.1137/S0036139995281822>.
- [19] M. BONNET, A. BUREL, M. DURUFLÉ, AND P. JOLY, *Effective transmission conditions for thin-layer transmission problems in elastodynamics. The case of a planar layer model*, Math. Model. Numer. Anal., 50 (2016), pp. 43–75, <https://doi.org/10.1051/m2an/2015030>.
- [20] C. CHNITI, S. ALHAZMI, S. ALTOUM, AND M. TOUJANI, *DtN and NtD surface radiation conditions for two-dimensional acoustic scattering: Formal derivation and numerical validation*, Appl. Numer. Math., 101 (2016), pp. 53–70, <https://doi.org/10.1016/j.apnum.2015.08.013>.
- [21] B. COX, S. ARRIDGE, AND P. BEARD, *Photoacoustic tomography with a limited-aperture planar sensor and a reverberant cavity*, Inverse Problems, 23 (2007), pp. S95–S112, <https://doi.org/10.1088/0266-5611/23/6/S08>.
- [22] B. COX, J. LAUFER, AND P. BEARD, *The challenges for quantitative photoacoustic imaging*, Proc. SPIE, 7177 (2009), pp. 1–9, <https://doi.org/10.1117/12.806788>.
- [23] B. COX, J. G. LAUFER, S. R. ARRIDGE, AND P. C. BEARD, *Quantitative spectroscopic photoacoustic imaging: A review*, J. Biomed. Opt., 17 (2012), pp. 061202–1–061202–22, <https://doi.org/10.1117/1.JBO.17.6.061202>.
- [24] B. T. COX AND P. C. BEARD, *The frequency-dependent directivity of a planar Fabry-Perot polymer film ultrasound sensor*, IEEE Trans. Ultrason. Ferroelectr. Freq. Control, 54 (2007), pp. 394–404, <https://doi.org/10.1109/TUFFC.2007.253>.
- [25] T. DING, K. REN, AND S. VALLÉLIAN, *A one-step reconstruction algorithm for quantitative photoacoustic imaging*, Inverse Problems, 31 (2015), 095005, <https://doi.org/10.1088/0266-5611/31/9/095005>.
- [26] M. P. DO CARMO, *Differential Geometry of Curves and Surfaces*, Prentice-Hall, Englewood Cliffs, NJ, 1976.
- [27] P. DRABEK AND J. MILOTA, *Methods of Nonlinear Analysis*, Birkhäuser Verlag, Basel, 2007, <https://doi.org/10.1007/978-3-7643-8147-9>.
- [28] R. ELLWOOD, E. ZHANG, P. BEARD, AND B. COX, *Photoacoustic imaging using reflectors to enhance planar arrays*, J. Biomed. Opt., 19 (2014), 126012, <https://doi.org/10.1117/1.JBO.19.12.126012>.
- [29] H. ENGL, M. HANKE, AND A. NEUBAUER, *Regularization of Inverse Problems*, Math. Appl. 375, Springer, New York, 2000.
- [30] L. C. EVANS, *Partial Differential Equations*, Grad. Stud. Math. 19, AMS, Providence, RI, 1998.
- [31] D. FINCH, *On a thermoacoustic transform*, in Proceedings of the 8th International Meeting on Fully 3D Image Reconstruction in Radiology and Nuclear Medicine, 2005, pp. 150–151.
- [32] C. FREDERICK, K. REN, AND S. VALLÉLIAN, *Image reconstruction in quantitative photoacoustic tomography with the simplified P2 approximation*, SIAM J. Imaging Sci., 11 (2018), pp. 2847–2876, <https://doi.org/10.1137/18m1195656>.
- [33] R. GLOWINSKI, J.-L. LIONS, AND J. HE, *Exact and Approximate Controllability for Distributed Parameter Systems: A Numerical Approach*, Encyclopedia Math. Appl. 117, Cambridge University Press, Cambridge, UK, 2008, <https://doi.org/10.1017/CBO9780511721595>.
- [34] J. A. GUGGENHEIM, E. Z. ZHANG, AND P. C. BEARD, *A method for measuring the directional response of ultrasound receivers in the range 0.3–80 MHz using a laser-generated ultrasound source*, IEEE Trans. Ultrason. Ferroelectr. Freq. Control, 64 (2017), pp. 1857–1863, <https://doi.org/10.1109/TUFFC.2017.2758173>.

- [35] M. HALTMEIER, R. KOWAR, AND L. V. NGUYEN, *Iterative methods for photoacoustic tomography in attenuating acoustic media*, *Inverse Problems*, 33 (2017), 115009, <https://doi.org/10.1088/1361-6420/aa8cba>.
- [36] M. HALTMEIER, L. NEUMANN, L. V. NGUYEN, AND S. RABANSER, *Analysis of the linearized problem of quantitative photoacoustic tomography*, *SIAM J. Appl. Math.*, 78 (2018), pp. 457–478, <https://doi.org/10.1137/16M1109291>.
- [37] M. HALTMEIER AND L. V. NGUYEN, *Analysis of iterative methods in photoacoustic tomography with variable sound speed*, *SIAM J. Imaging Sci.*, 10 (2017), pp. 751–781, <https://doi.org/10.1137/16M1104822>.
- [38] Y. HRISTOVA, P. KUCHMENT, AND L. NGUYEN, *Reconstruction and time reversal in thermoacoustic tomography in acoustically homogeneous and inhomogeneous media*, *Inverse Problems*, 24 (2008), 055006, <https://doi.org/10.1088/0266-5611/24/5/055006>.
- [39] B. HUANG, J. XIA, K. MASLOV, AND L. WANG, *Improving limited-view photoacoustic tomography with an acoustic reflector*, *J. Biomed. Opt.*, 18 (2013), 110505, <https://doi.org/10.1117/1.JBO.18.11.110505>.
- [40] C. HUANG, K. WANG, L. NIE, L. WANG, AND M. ANASTASIO, *Full-wave iterative image reconstruction in photoacoustic tomography with acoustically inhomogeneous media*, *IEEE Trans. Medical Imaging*, 32 (2013), pp. 1097–1110, <https://doi.org/10.1109/TMI.2013.2254496>.
- [41] M. JOHANSSON, P. FOLKOW, A. HÄGGLUND, AND P. OLSSON, *Approximate boundary conditions for a fluid-loaded elastic plate*, *J. Acoust. Soc. America*, 118 (2005), pp. 3436–3446, <https://doi.org/10.1121/1.2126927>.
- [42] R. KOWAR AND O. SCHERZER, *Photoacoustic imaging taking into account attenuation*, in *Mathematical Modeling in Biomedical Imaging II*, Springer, New York, 2011, pp. 85–130.
- [43] R. KRESS, *Linear Integral Equations*, 2nd ed., *Appl. Math. Sci.* 82, Springer, New York, 1999.
- [44] P. KUCHMENT AND L. KUNYANSKY, *Mathematics of thermoacoustic tomography*, *European J. Appl. Math.*, 19 (2008), pp. 191–224, <https://doi.org/10.1017/S0956792508007353>.
- [45] L. KUNYANSKY, B. HOLMAN, AND B. COX, *Photoacoustic tomography in a rectangular reflecting cavity*, *Inverse Problems*, 29 (2013), 125010, <https://doi.org/10.1088/0266-5611/29/12/125010>.
- [46] I. LASIECKA, J.-L. LIONS, AND R. TRIGGIANI, *Nonhomogeneous boundary value problems for second order hyperbolic equations*, *J. Math. Pures Appl.*, 65 (1986), pp. 149–192.
- [47] J.-L. LIONS AND E. MAGENES, *Non-Homogeneous Boundary Value Problems and Applications*, Vol. I, *Grundlehren Math. Wiss.* 181, Springer, Berlin, 1972.
- [48] J.-L. LIONS AND E. MAGENES, *Non-Homogeneous Boundary Value Problems and Applications*, Vol. II, *Grundlehren Math. Wiss.* 182, Springer, Berlin, 1972.
- [49] J.-L. LIONS AND E. MAGENES, *Non-Homogeneous Boundary Value Problems and Applications*, Vol. III, *Grundlehren Math. Wiss.* 183, Springer, Berlin, 1972.
- [50] W. MCLEAN, *Strongly Elliptic Systems and Boundary Integral Equations*, Cambridge University Press, Cambridge, UK, 2000.
- [51] D. MODGIL, M. ANASTASIO, AND P. LA RIVIÈRE, *Image reconstruction in photoacoustic tomography with variable speed of sound using a higher-order geometrical acoustics approximation*, *J. Biomed. Opt.*, 15 (2010), 021308, <https://doi.org/10.1117/1.3333550>.
- [52] L. NGUYEN AND L. KUNYANSKY, *A dissipative time reversal technique for photo-acoustic tomography in a cavity*, *SIAM J. Imaging Sci.*, 9 (2016), pp. 748–769, <https://doi.org/10.1137/15M1049683>.
- [53] L. V. NGUYEN, *A family of inversion formulas in thermoacoustic tomography*, *Inverse Problems Imaging*, 3 (2009), pp. 649–675, <https://doi.org/10.3934/ipi.2009.3.649>.
- [54] L. V. NGUYEN AND M. HALTMEIER, *Reconstruction Algorithms for Photoacoustic Tomography in Heterogeneous Damping Media*, [arXiv:1808.06176](https://arxiv.org/abs/1808.06176), 2018.
- [55] R. NUSTER, S. GRATT, K. PASSLER, H. GRÜN, T. BERER, P. BURGHOLZER, AND G. PALTAUF, *Comparison of optical and piezoelectric integrating line detectors*, in *Biomedical Optics: Photons Plus Ultrasound: Imaging and Sensing*, Proc. SPIE 7177, Bellingham, WA, 2009, <https://doi.org/10.1117/12.808873>.
- [56] R. NUSTER AND G. PALTAUF, *Comparison of piezoelectric and optical projection imaging for three-dimensional in vivo photoacoustic tomography*, *J. Imaging*, 5 (2019), 15, <https://doi.org/10.3390/jimaging5010015>.
- [57] B. PALACIOS, *Reconstruction for multi-wave imaging in attenuating media with large damping coefficient*, *Inverse Problems*, 32 (2016), 125008, <https://doi.org/10.1088/0266-5611/32/12/125008>.

- [58] G. PALTAUF, P. HARTMAIR, G. KOVACHEV, AND R. NUSTER, *Piezoelectric line detector array for photoacoustic tomography*, *Photoacoustics*, 8 (2017), pp. 28–36, <https://doi.org/10.1016/j.pacs.2017.09.002>.
- [59] V. PÉRON, *Equivalent boundary conditions for an elasto-acoustic problem set in a domain with a thin layer*, *Math. Model. Numer. Anal.*, 48 (2014), pp. 1431–1449, <https://doi.org/10.1051/m2an/2014002>.
- [60] M. PRAMANIK AND L. WANG, *Thermoacoustic and photoacoustic sensing of temperature*, *J. Biomed. Opt.*, 14 (2009), 054024, <https://doi.org/10.1117/1.3247155>.
- [61] J. QIAN, P. STEFANOV, G. UHLMANN, AND H. ZHAO, *An efficient Neumann series-based algorithm for thermoacoustic and photoacoustic tomography with variable sound speed*, *SIAM J. Imaging Sci.*, 4 (2011), pp. 850–883, <https://doi.org/10.1137/100817280>.
- [62] K. REN AND F. TRIKI, *A global stability estimate for the photo-acoustic inverse problem in layered media*, *European J. Appl. Math.*, (2018), pp. 1–24, <https://doi.org/10.1017/S0956792518000268>.
- [63] O. SCHERZER AND C. SHI, *Reconstruction formulas for photoacoustic imaging in attenuating media*, *Inverse Problems*, 34 (2017), 015006, <https://doi.org/10.1088/1361-6420/aa9ade>.
- [64] C. SHEAFF AND S. ASHKENAZI, *Characterization of an improved Polyimide-Etalon all-optical transducer for high-resolution ultrasound imaging*, *IEEE Trans. Ultrason. Ferroelectr. Freq. Control*, 61 (2014), pp. 1223–1232, <https://doi.org/10.1109/TUFFC.2014.3021>.
- [65] P. STEFANOV AND G. UHLMANN, *Thermoacoustic tomography with variable sound speed*, *Inverse Problems*, 25 (2009), 075011, <https://doi.org/10.1088/0266-5611/25/7/075011>.
- [66] P. STEFANOV AND Y. YANG, *Multiwave tomography with reflectors: Landweber’s iteration*, *Inverse Problems Imaging*, 11 (2017), pp. 373–401, <https://doi.org/10.3934/ipi.2017018>.
- [67] K. WANG AND M. ANASTASIO, *Photoacoustic and thermoacoustic tomography: Image formation principles*, in *Handbook of Mathematical Methods in Imaging*, O. Scherzer, ed., Springer, New York, 2011, pp. 781–815.
- [68] K. WANG, S. ERMILOV, R. SU, H. BRECHT, A. ORAEVSKY, AND M. ANASTASIO, *Imaging model incorporating ultrasonic transducer properties for three-dimensional optoacoustic tomography*, *IEEE Trans. Medical Imaging*, 30 (2011), pp. 203–214, <https://doi.org/10.1109/TMI.2010.2072514>.
- [69] K. WANG, C. HUANG, Y.-J. KAO, C.-Y. CHOU, A. ORAEVSKY, AND M. ANASTASIO, *Accelerating image reconstruction in three-dimensional optoacoustic tomography on graphics processing units*, *Medical Phys.*, 40 (2013), 023301, <https://doi.org/10.1118/1.4774361>.
- [70] K. WANG, R. SU, A. ORAEVSKY, AND M. ANASTASIO, *Investigation of iterative image reconstruction in three-dimensional optoacoustic tomography*, *Phys. Medicine Biol.*, 57 (2012), pp. 5399–5423, <https://doi.org/10.1088/0031-9155/57/17/5399>.
- [71] L. V. WANG, *Photoacoustic Imaging and Spectroscopy*, CRC Press, Boca Raton, FL, 2009.
- [72] L. V. WANG AND S. HU, *Photoacoustic tomography: In vivo imaging from organelles to organs*, *Science*, 335 (2012), pp. 1458–1462, <https://doi.org/10.1126/science.1216210>.
- [73] L. V. WANG AND H. WU, *Biomedical optics: Principles and Imaging*, Wiley-Interscience, Hoboken, NJ, 2007, <https://doi.org/10.1002/9780470177013>.
- [74] X. WANG, Y. PANG, G. KU, X. XIE, G. STOICA, AND L. V. WANG, *Noninvasive laser-induced photoacoustic tomography for structural and functional in vivo imaging of the brain*, *Nature Biotechnol.*, 21 (2003), pp. 803–806, <https://doi.org/10.1038/nbt839>.
- [75] V. WILKENS AND W. MOLKENSTRUCK, *Broadband PVDF membrane hydrophone for comparisons of hydrophone calibration methods up to 140 MHz*, *IEEE Trans. Ultrason. Ferroelectr. Freq. Control*, 54 (2007), pp. 1784–1791, <https://doi.org/10.1109/TUFFC.2007.462>.
- [76] J. XIA, J. YAO, AND L. V. WANG, *Photoacoustic tomography: Principles and advances*, *Electromagn. Waves (Camb.)*, 147 (2014), pp. 1–22.
- [77] M. XU AND L. V. WANG, *Analytic explanation of spatial resolution related to bandwidth and detector aperture size in thermoacoustic or photoacoustic reconstruction*, *Phys. Rev. E*, 67 (2003), 056605, <https://doi.org/10.1103/PhysRevE.67.056605>.
- [78] Y. XU AND L. V. WANG, *Effects of acoustic heterogeneity in breast thermoacoustic tomography*, *IEEE Trans. Ultrason. Ferroelectr. Freq. Control*, 50 (2003), pp. 1134–1146.
- [79] Y. XU AND L. V. WANG, *Time reversal and its application to tomography with diffracting sources*, *Phys. Rev. Lett.*, 92 (2004), 033902, <https://doi.org/10.1103/PhysRevLett.92.033902>.

- [80] G. YOO, H. YOON, J. HEO, U. K. THAKUR, H. J. PARK, H. W. BAAC, AND J. HEO, *All-optical ultrasound transducer using CNT-PDMS and Etalon thin-film structure*, IEEE Photonics J., 7 (2015), 6803708, <https://doi.org/10.1109/JPHOT.2015.2496862>.
- [81] G. ZANGERL, S. MOON, AND M. HALTMEIER, *Photoacoustic Tomography with Direction Dependent Data: An Exact Series Reconstruction Approach*, arXiv:1812.09545, 2018.
- [82] E. ZHANG, J. LAUFER, AND P. BEARD, *Backward-mode multiwavelength photoacoustic scanner using a planar Fabry-Perot polymer film ultrasound sensor for high-resolution three-dimensional imaging of biological tissues*, Appl. Opt., 47 (2008), pp. 561–577, <https://doi.org/10.1364/AO.47.000561>.